# Mechanistic Insights on the Low Temperature Oxidation of CO Catalyzed by Isolated Co Ions in N-doped Carbon

Colby A. Whitcomb, <sup>1</sup> Anna Sviripa, <sup>1</sup> Michael I. Schapowal, <sup>1</sup> Konstantin Mamedov, <sup>1</sup> Raymond R. Unocic, <sup>2</sup> Christopher Paolucci, <sup>1\*</sup> and Robert J. Davis <sup>1\*</sup>

<sup>1</sup>Department of Chemical Engineering, University of Virginia, Charlottesville, Virginia 22903, United States

<sup>2</sup>Center for Nanophase Materials Sciences, Oak Ridge National Laboratory, Oak Ridge, TN 37831, United States

\*rjd4f@virginia.edu \*cp9wx@virginia.edu

<sup>\*</sup>Corresponding authors emails: rjd4f@virginia.edu; cp9wx@virginia.edu

#### **Abstract**

Isolated cobalt ions on nitrogen-doped carbon (Co-N-C) catalyze CO oxidation at temperatures as low as 196 K, but the active site and mechanism for this reaction remain elusive. In this work, steady-state CO oxidation around 273 K over Co-N-C revealed nearly first order behavior in both CO and  $O_2$  as well as a negative apparent activation energy. Isotopic transient analysis of the reaction confirmed a rapid turnover frequency and low surface coverage of adsorbed intermediates leading to  $CO_2$  (< 10% of the Co). Results from kinetics experiments combined with quantum chemical calculations and molecular dynamics simulations are consistent with a reaction path involving weak adsorption of CO onto Co ions followed by a low barrier for the CO-assisted activation of weakly adsorbed  $O_2$ . This proposed mechanism for dioxygen activation does not involve a redox cycle with the transition metal ion and may be important in other low temperature catalytic reactions involving  $O_2$ .

# **Keywords**

CO oxidation; N-Doped carbon; heterogenous catalysis; density functional theory; SSITKA; AIMD

#### 1. Introduction

Transition metal ions (M) isolated in a nitrogen-doped carbon matrix (M-N-C) have demonstrated high activity for both electrocatalytic 1-7 and thermocatalytic 1-2 reactions with molecular oxygen. Some of these M-N-C materials even exhibit activity and selectivity comparable to expensive Pt-based electrodes in the electrochemical oxygen reduction reaction (ORR) and Pt nanoparticles in the catalytic oxidative dehydrogenation of alcohols. 1, 2, 8-10, 13 Although M-N-C catalysts facilitate both thermal and electrochemical reactions involving dioxygen activation, both the coordination environment around the isolated metal center and the mechanism for dioxygen activation remain controversial. 8-10

To investigate O<sub>2</sub> activation over M-N-C catalysts in the absence of the complicating effects of solvents and applied potentials, gas phase oxidation of CO by O2 has been used. Catalytic CO oxidation was recently investigated on Fe-N-C, Co-N-C, and materials containing both Co and Fe (Co, Fe-N-C), with the Co-containing samples promoting oxidation catalysis even at dry-ice acetone temperatures.<sup>14</sup> The reported high conversion achieved at low temperature over Co, Fe-N-C specifically was attributed to the relatively weak but preferential binding of CO to Co simultaneous with O<sub>2</sub> binding on nearby Fe.<sup>14</sup> Strasser and co-workers confirmed with cryo-CO chemisorption measurements that CO indeed adsorbs on Fe and FeNi M-N-C type catalysts strongly while other metals such as Ni catalysts exhibit low heats of adsorption.<sup>15, 16</sup> In the well-studied catalytic oxidation of CO on transition metal particles such as Pt and Pd, chemisorption of reactants to the metal prior to surface reaction is required to form product CO<sub>2</sub> in a Langmuir-Hinshelwood type mechanism (LH).<sup>17, 18</sup> The strong binding of CO to platinum group metals restricts the use of nanoparticle-based catalysts to higher temperatures for CO oxidation as competitive adsorption of CO at lower temperature actually inhibits catalytic turnover.<sup>18</sup> Other potential reaction paths for CO oxidation are of the Eley-Rideal (ER) type (involving reaction of a gas phase species with an adsorbed species) and the Mars-van Krevelen-type (MvK) (involving transfer of lattice oxygen followed by re-oxidation of the lattice). 19, 20 Very recently, results of studies with isolated Ir atoms supported on Mg/Al<sub>2</sub>O<sub>4</sub> are consistent with an interesting mechanism involving a spectator CO molecule binding to the Ir site, while the CO oxidation reaction proceeds through an ER type mechanism involving surface oxygen.<sup>21</sup> Low temperature CO oxidation has also been reported to occur on Au nanoparticles supported on reducible oxides where CO binds weakly to Au and the reducible oxide support is involved in the activation of O<sub>2</sub>, which can be considered to occur through an MvK-type mechanism.<sup>22-24</sup>

Some unique formulations of Co oxides also demonstrate catalytic activity in CO oxidation at subambient temperature and the reaction is proposed to occur through an MvK mechanism.  $^{25-27}$  The catalytic cycle is hypothesized to proceed through a  $Co^{3+}$  /  $Co^{2+}$  redox cycle involving labile  $O^{2-}$  sites from the support.  $^{27-29}$  As the Co-N-C catalysts with isolated  $Co^{2+}$  ions lack labile  $O^{2-}$  sites, as well as sites containing multiple Co ions required to activate  $O_2$  through a standard redox process, it is unclear how CO oxidation might occur through a redox cycle on these materials. Given the unusual behavior of a nominally single site M-N-C catalyst that can activate  $O_2$  at temperatures as low as 196 K, there is a need for a molecularly detailed understanding of the reaction mechanism.

Here, we explore a potential mechanism of low temperature CO oxidation on Co-N-C catalysts using steady-state and transient kinetic experiments, quantum chemical calculations, and molecular dynamics simulations. Our experimental and computational results are consistent with a mechanism for  $O_2$  activation involving interactions with weakly adsorbed CO on the Co-N-C catalyst, emphasizing the important role of co-adsorbates in surface-catalyzed reactions. This proposed mechanism differs from previously described strong binding systems that utilize support oxygen species and redox cycles to catalyze reactions involving  $O_2$  activation.

#### 2. Methods

Synthesis of Co catalysts. The Co-N-C catalyst was synthesized via a modified method of high temperature pyrolysis similar to previously reported methods. 8, 9, 30 Cobalt nitrate hexahydrate (0.492 g) (Sigma-Aldrich Corporation) was dissolved in 10 cm<sup>3</sup> of distilled, de-ionized (DDI) H<sub>2</sub>O and added to a solution of 1,10 phenanthroline (0.611 g) (Sigma-Aldrich Corporation) in 15 cm<sup>3</sup> ethanol (Sigma-Aldrich Corporation) to make a 1:2 molar ratio of Co: phenanthroline before stirring for 20 min at 353 K. This mixture was subsequently added dropwise to a 0.1 M NaOH slurry with Carbon Black Pearls 2000 (Cabot Corporation) at 353 K and stirred for 2 h. The slurry was then washed with 3000 cm3 of DDI H2O and vacuum filtered before drying overnight at 343 K. The sample with deposited Co phenanthroline complex was then impregnated with 80 wt % dicyandiamide relative to the complex. The solution was vigorously stirred at 343 K and then dried overnight. The impregnated sample was subsequently ramped in ultra-high purity (UHP)  $N_2$  (100 cm<sup>3</sup> min<sup>-1</sup>) (99.999 %, Praxair) at 10 K min<sup>-1</sup> and then held at 973 K for a high temperature thermal treatment. To ensure removal of nanoparticles, the Co-N-C catalyst (100 mg) was then acid washed with a vigorously stirred 1 M HCl solution (100 cm<sup>3</sup>) at room-temperature for 12 h. The acid washed catalyst was then thoroughly washed and filtered before drying overnight at 343 K. To reduce the possibility of CI ions being deposited on the surface, a second thermal treatment was conducted. The catalyst was ramped at 10 K min<sup>-1</sup> to 673 K and held for 2 h in flowing UHP  $H_2$  (100 cm<sup>3</sup> min<sup>-1</sup>) (5 %  $H_2$ /Ar). This catalyst was subsequentially used as synthesized. The nitrogen-carbon (N-C) catalyst without metal was synthesized via impregnation of an aqueous solution of 0.4 g dicyandiamide (Sigma-Aldrich) into 0.5 g of Carbon Black Pearls 2000 using the same thermal treatment method described above for the metal loaded catalyst. The 5 wt % CoO<sub>x</sub>/SiO<sub>2</sub> catalyst was synthesized by incipient wetness impregnation wherein cobalt nitrate hexahydrate (0.5 g) was dissolved in 2.5 cm<sup>3</sup> of DDI H<sub>2</sub>O and added dropwise to silica gel (2 g) (Davisil 636 Silica Gel).<sup>31, 32</sup> The catalyst was then dried overnight at room temperature before drying for two hours in an oven at 393 K. The catalyst was then ramped at 10 K min<sup>-1</sup> to 673 K and thermally treated for 2 h in flowing air (Medical Grade, Praxair). The 10 wt % Co/CB catalyst was synthesized by incipient wetness impregnation of cobalt acetate (0.04 g, Aldrich) dissolved in 1 cm<sup>3</sup> DDI H<sub>2</sub>O onto Carbon Black Pearls 2000 (0.2 g). The mixture was then dried at 393 K overnight. The catalyst was then thermally treated at 973 K for two hours after ramping at 10 K min<sup>-1</sup> in UHP He (99.999 %, Praxair). The Co<sub>3</sub>O<sub>4</sub> (Co (II, III) Oxide, Alfa Aesar) was used from the bottle and thermally treated for 5 hours at 673 K in 100 cm<sup>3</sup> min<sup>-1</sup> flowing air after ramping at 10 K min<sup>-1</sup>.

**Characterization of Catalysts**. High-angle annular dark-field STEM imaging was performed using an aberration-corrected STEM JEOL NeoARM, operating at 80 kV and using a convergence semi-angle of 27 mrad.

All inductively coupled plasma optical emission spectroscopy (ICP) analyses were completed at Galbraith Laboratories Inc. (2323 Sycamore Drive, Knoxville, TN 37921). The metal loadings of the Co catalysts were determined using ICP-OES on a PerkinElmer Optima 5300V, 8300DV, or Avio 500 ICP-OES.

X-ray photoelectron spectroscopy (XPS) measurements were performed using a PHI VersaProbe III spectrometer equipped with a Monochromatic Al k-alpha X-rays (1486.6 eV) and a hemispherical analyzer. A 1400  $\mu$ m sample spot size was utilized with a pass energy of 55 eV and an X-ray beam size of 100  $\mu$ m for high resolution region scans. A dual neutralization system consisting of an internal electron flood gun (1 eV) and a low energy Ar ion gun was utilized during data collection. Binding energies for all elements were referenced to the C 1s peak at 284.8 eV.

X-ray absorption spectroscopy (XAS) at the Co K edge was performed on beamline 8-ID at the National Synchrotron Light Source II at Brookhaven National Laboratory with a ring energy of 3.0 GeV and a beam current of 400 mA. A Co metal foil (Goodfellow Corporation) was used as a reference for the Co (7709 eV) K edge. Samples were prepared by dilution of catalyst in boron nitride and adjusted to provide an adsorption edge jump of close to unity. The spectra were collected by utilizing a temperature-controlled transmission cell previously described.<sup>33</sup> A flow of H<sub>2</sub> or CO at 10 cm<sup>3</sup> min<sup>-1</sup> was flowed over the samples that were enclosed in the Kapton window chambers. The XAS data were processed using the Demeter software package.<sup>34</sup> The Co-N amplitude reduction factor was obtained from Xie et al. using Co phthalocyanine as a reference material at the same beamline.<sup>9</sup>

Oxidation of CO. The oxidation of CO was carried out in a stainless-steel, down flow, continuous packed bed reactor (Fig. S1). The catalyst was diluted with 0.25 g of SiC (Universal Photonoics, Inc., 150 mesh) for each reaction. Reaction conditions were:  $160 \text{ cm}^3 \text{ min}^{-1}$  total gas flow with 1 % CO (Praxair 4 % CO/He), 1 % or 13 % O<sub>2</sub> (Praxair 20 % O<sub>2</sub>/He), 1 % Ar (Praxair UHP, 99.999 %), and balance He (Praxair UHP, 99.999 %) at 3 atm. The He, Ar, and H<sub>2</sub> lines were passed through OMI-2 indicator filters while the CO and O<sub>2</sub> gases were purified through silica traps in a dry ice-acetone bath. Prior to any reaction run, the catalyst was thermally pretreated in situ by ramping at 10 % K min<sup>-1</sup> to 673 % and held for 2 % h in He before cooling to the reaction temperature. The reactor effluent was analyzed using a Balzers Quadrupole Mass Spectrometer. Signals associated with masses (m/e) 28, 29, 40, 44, and 45 amu were recorded at a voltage of 1200 % and dwell times of 50 % ms for all masses except 44 % and 45 %, which were measured at 100 %.

Steady-State Isotopic Transient Kinetic Analysis. Transient kinetic experiments were conducted using the same reactor setup and gas flows as for the oxidation of CO (Fig. S1). The Co-N-C catalyst (0.03 g) was loaded with SiC diluent (0.25 g) into the packed bed reactor. A pretreatment in flowing He at 673 K was done before cooling to 273 K for the SSITKA experiments. A full explanation of the methodology for SSITKA can be found in the review by Shannon and Goodwin. Briefly, integration of the area between the normalized transient responses,  $F_i$ , of product  $^{12}CO_2$  or  $^{13}CO_2$  and Ar (to account for the gas phase holdup of the system) following a switch at equal temperature and pressure allows for the average residence time of surface intermediates leading to product,  $\tau$ , to be calculated according to:

$$\tau = \int_0^\infty \left[ F_{12_{CO_2}} - F_{Ar} \right] dt \tag{1}$$

The  $\tau$  determined from the transient response of the product can also include the influence of readsorption on the catalyst prior to exiting the reactor, causing the calculated  $\tau$  for CO<sub>2</sub> production to be a convolution of the intrinsic kinetics of the CO oxidation reaction and a time delay caused by re-adsorption on the catalyst. Evaluation of  $\tau$  at various flow rates can be helpful to determine if product re-adsorption in the catalyst bed is affecting the measurement.<sup>35, 36</sup> According to Fig. S2 a and b, the conversion of the CO oxidation reaction was strictly proportional to the inverse of the flow rate, confirming the rate of reaction was constant over the range of conversions and flow rates used.

Density Functional Theory Calculations. We performed spin-polarized periodic supercell density functional theory (DFT) calculations with a plane wave basis set and an energy cutoff of 500 eV using the Vienna ab initio simulation package (VASP)<sup>37</sup> version 5.4.4. All structures were converged to a criterion of 10<sup>-6</sup> eV and 0.01 eV/Å for self-consistent-field (SCF) energies and atomic forces, respectively. We used a 8.5 Å x 9.8 Å graphene supercell with 14 Å vacuum in the z-direction with two vacancies for a total of 31 C atoms (when the number of nitrogen atoms is zero) as well as zero to four pyridinic N atoms and a Co atom (corresponding to a density of 1.2 Co nm<sup>2</sup>). All structure files are provided as a supporting information attachment. Monkhorst-Pack k-points were used with a 4 x 4 x 1 mesh. We considered multiple binding modes (e.g. monodentate and bidentate O<sub>2</sub> on Co) and spin states for each structure; all structure files are included as a supporting information attachment. To test the sensitivity of our results to the cell size and Co density in the supercell we computed CO and O₂ binding energies in larger supercells that contained 1-2 Co atoms (Table S1) and found they were insensitive to the Co density in the supercell between 0.3 - 1.2 Co nm<sup>2</sup>. We report only energies and not free energies because the reaction intermediates are weakly adsorbed and not amenable to standard free energy approximations. To reduce computational cost, we neglected vibrational zero-point energy corrections, which are expected to have a negligible contribution to our reaction energies for this system.

Recent reports on similar structures  $^{38,39}$  indicate that reaction energies for these materials are sensitive to functional choice. Therefore, the gas phase CO oxidation reaction energy (Table S2), CO and  $O_2$  binding energies, and reaction mechanism calculations were performed with a variety of commonly used functionals (Table S3). The CO and  $O_2$  binding energies on  $CoN_4$  vary from -92 to -50 kJ  $mol^{-1}$ , and -82 to -57 kJ  $mol^{-1}$ , respectively, depending on the choice of DFT functional (Table S3). However, the trend of more endothermic binding energies with increasing N substitution is preserved across all functionals. We chose to report the values computed with the vdW-DF functional  $^{40}$  in the main text because this functional accounts for nonlocal electron correlation dispersion interactions (important for weak adsorption), reproduces the experimental enthalpy of reaction for gas phase CO oxidation as reported in Table S2, and the experimental CO binding energy determined by microcalorimetry  $^{14}$  (-58.8 kJ  $mol^{-1}$ ) on Co-N-C materials with isolated Co sites.  $^{14}$  For comparison we also report the corresponding PBE-D3 $^{41}$  and vdW-DF2 $^{42}$  reaction coordinate diagrams in Fig. S3.

Transition states were determined using climbing image nudged elastic band (CI-NEB) calculations per the method of Henkelman et al.,  $^{43,44}$  and are reported in Fig. S4. We calculated TS1 with various spin states and found that although the barrier is sensitive to the choice of spin, and generally decreases with lower spin, the reactant energy varies only weakly with spin state. Therefore, we report the low spin reaction coordinate (magnetic moment = 0) for the reaction corresponding to TS1.

**AIMD Simulations**. For the AIMD simulations we used the PBE-D3 functional for two reasons: 1) it is much less computationally expensive than vdW-DF, and 2) CO and  $O_2$  binding energies are more exothermic with PBE-D3 than vdW-DF (Table S3), which enabled us to run the simulations at temperatures high enough (398 K) to frequently overcome low energy barriers without desorption of the reactants. This temperature is still low enough that direct dissociation of  $O_2$  over Co during the AIMD simulation would be prohibitive based on the 66 kJ mol<sup>-1</sup> barrier computed with PBE.<sup>45</sup> Figure S5 reports the free energies during the AIMD simulations and structural snapshots. Movies and structures for the full trajectories are provided as a supporting information attachment. All AIMD simulations were run in VASP version 5.4.4 at 398 K using a Nose-Hoover thermostat with a time step of 0.5 fs.

# 3. Results

Catalyst synthesis and characterization. The 1.89 wt % Co-N-C catalyst was synthesized using a modified high temperature pyrolysis method in  $N_2$ . To disperse Co ions in Co-N-C and remove residual nanoparticles, treatment in mild acid solution followed by high temperature treatment in  $H_2$  was conducted. To confirm the presence of isolated Co ions on Co-N-C, we examined the sample by atomic resolution high-angle annular dark-field scanning transmission electron microscopy (HAADF-STEM) which is shown in Fig. 1. We did not observe any Co nanoparticles, indicating that washing a freshly pyrolyzed sample in mild acid solution was effective at removing Co nanoparticles without removing Co ions present in the N-C support.

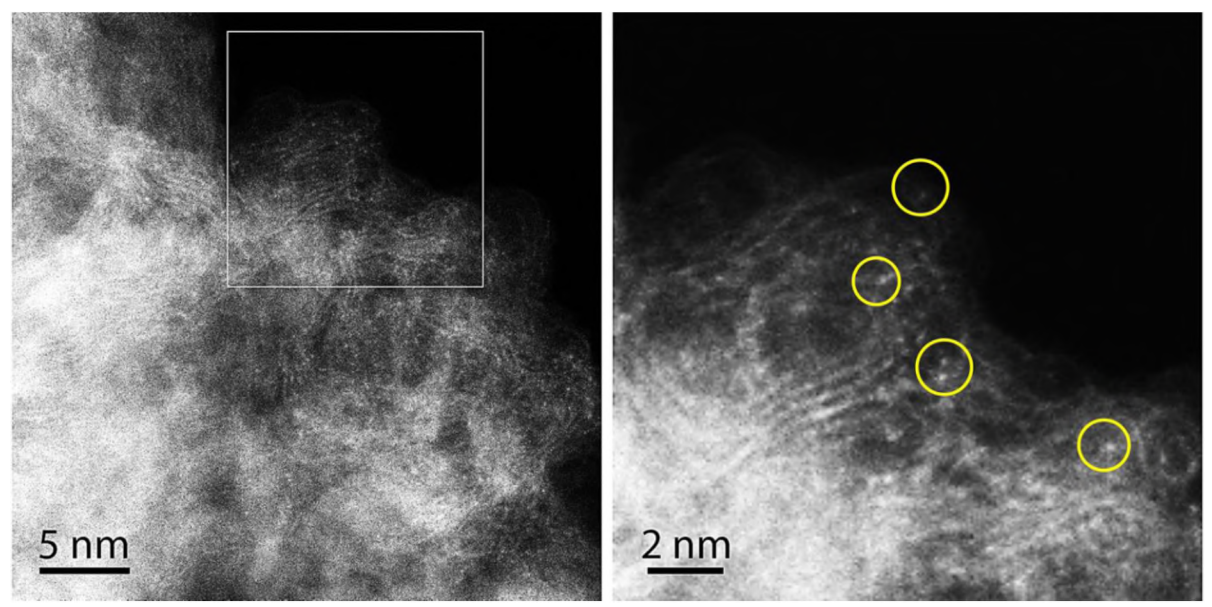


**Figure 1.** Atomic resolution HAADF-STEM images of Co-N-C show single atom distribution of Co atoms. The right panel is an inset of the boxed area in the left panel. The Co atoms in the expanded area are circled in yellow.

X-ray photoelectron spectroscopy (XPS) was used to determine the chemical state of the Co and N in the catalyst. Spectra associated with the Co  $2p_{3/2}$  and the N 1s regions are shown in Figs. S6 and S7, respectively. The presence of a major peak at a binding energy (BE) of 780.9 eV in the Co  $2p_{3/2}$  spectrum accompanied by a satellite peak at 785.9 eV at one-third the intensity is consistent with  $Co^{2+}$ . Multiple forms of N are usually observed by XPS of similar materials, including pyridinic (BE=398 eV), pyrrolic (BE=400 eV), and graphitic (BE=401 eV), with pyridinic being commonly associated with formation of the Co active site (Fig. S7). A8, A9 Table S4 shows that the molar ratio of pyridinic N relative to  $Co^{2+}$  is  $Co^{2+}$  10:1, which suggests there is sufficient pyridinic N content to form commonly proposed  $CoN_x$  sites  $Co^{2+}$  10:1, which suggests there is sufficient pyridinic N content to form commonly proposed  $CoN_x$  sites  $Co^{2+}$  10:1, which suggests there is sufficient pyridinic N content to form commonly proposed  $CoN_x$  sites  $Co^{2+}$  10:1, which suggests there is sufficient pyridinic N content to form commonly proposed  $CoN_x$  sites  $Co^{2+}$  10:1, which suggests there is sufficient pyridinic N content to form commonly proposed  $CoN_x$  sites  $Co^{2+}$  10:1, which suggests there is sufficient pyridinic N content to form commonly proposed  $CoN_x$  sites  $Co^{2+}$  10:1, which suggests there is sufficient pyridinic N content to form commonly proposed  $CoN_x$  sites  $Co^{2+}$  10:1, which suggests there is sufficient pyridinic N content to form commonly proposed  $CoN_x$  sites  $Co^{2+}$  10:1, which suggests there is sufficient pyridinic N content to form commonly proposed  $CoN_x$  10:1, which suggests there is sufficient pyridinic N content to form commonly proposed  $CoN_x$  10:1, which suggests there is sufficient pyridinic N content to form commonly proposed  $CoN_x$  10:1, which suggests the content  $CoN_x$  10:1, which suggests there is sufficient pyridinic N content  $CoN_x$  10:1, which

X-ray absorption spectroscopy (summarized in Fig. 2 and Table 1) suggest the majority of the Co is bound to  $^{\sim}4$  N atoms, which is consistent with earlier work.

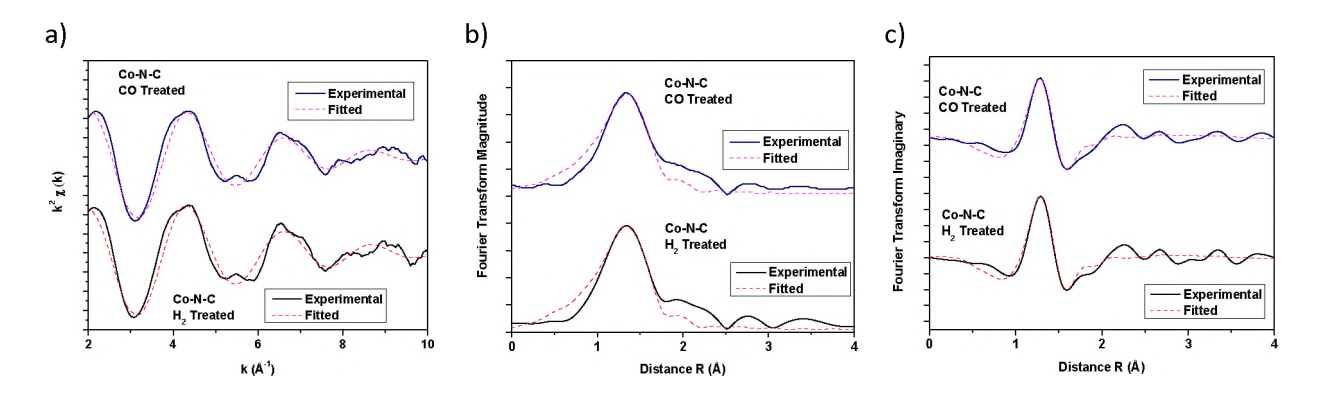


Figure 2. Fitting of the extended X-ray absorption fine structure (EXAFS) region of the Co K edge for the Co-N-C catalyst. a) Contributions of the Co-N path fitted in k space for Co-N-C during  $H_2$  or CO flows (10 cm<sup>3</sup> min<sup>-1</sup>). The catalyst was initially ramped in  $H_2$  to 738 K and held for 2 hours before cooling to 303 K. b) Fourier transforms (Experimental and Fitted) of  $k^2$ -weighted Co EXAFS for Co-N-C under flowing  $H_2$  or CO. c) Imaginary components (Experimental and Fitted) of the Fourier transform of  $k^2$ -weighted Co-N-C EXAFS obtained under flowing  $H_2$  or CO.

Table 1. Results of the analysis of Co EXAFS on Co-N-C during H₂ or CO flow<sup>a</sup>

Conditions	Shell	CN	r (Å)	$\Delta \sigma^2 (\mathring{A}^2)$	$\Delta E_{o}$ (eV)
H <sub>2</sub>	Co-N	4.9 ± 1.6	1.92 ± 0.03	0.01 ± 0.005	-3.2 ± 3.7
СО	Co-N	4.8 ± 1.8	1.93 ± 0.04	0.01 ± 0.01	-1.9 ± 4.3

<sup>a</sup> Fitting parameters: Fourier transform range,  $\Delta k$ , 1.5-10 Å<sup>-1</sup>; fitting range  $\Delta R$ , 1-2 Å;  $k^2$  weighting,  $S_o^2$  (Co-N) = 0.775 (obtained from Xie et al. using Co phthalocyanine as a reference material). <sup>9</sup> The Co-N-C catalyst was initially ramped in H<sub>2</sub> at 10 K min<sup>-1</sup> to 738 K and held for two hours before cooling to 303 K in H<sub>2</sub>.

Oxidation of CO over Co catalysts. To determine the effect of support composition on catalytic performance, the oxidation of CO was evaluated over a variety of supported Co catalysts over a range of temperatures (273 – 453 K) at a total pressure of 3 atm. The total pressure of 3 atm was achieved by adding He gas to substantially lower partial pressures of CO and  $O_2$  so that pressure transients often observed during isotopic transient experiments could be eliminated. All reaction kinetics reported here were evaluated in the steady-state regime. Oxidation of CO was not observed over an N-C sample that was prepared in the absence of the Co precursor, which illustrates the importance of the Co component in the reaction. In addition to Co-N-C, various other Co-containing catalysts were investigated, including highly dispersed 4.78 wt % Co/SiO<sub>2</sub>, nitrogen-free 2.29 wt % Co supported on carbon black (Co/CB), and Co oxide (Co<sub>3</sub>O<sub>4</sub>). Figure 3 illustrates the excellent catalytic performance of Co-N-C relative to the other Co catalysts at temperatures < 340 K, with the conversion of CO actually increasing with decreasing temperature for Co-N-C.

Multiple groups have reported on low temperature CO oxidation catalyzed by Co oxide structures.<sup>28, 29, 51, 52</sup> For example, Schüth and co-workers previously showed that CO oxidation can occur on uniquely shaped small Co oxide structures at temperatures as low as 196 K, while Haruta and coworkers found that Co spinel structures were also active at temperatures ranging from 198 to 323 K.<sup>27, 28</sup> The interesting "U" shape of the CO conversion with temperature (Fig. 3) observed for our Co-N-C catalyst is reminiscent of results for some Co oxide samples reported earlier.<sup>27, 51</sup> In previous work on Co oxide, a similar "U" shaped conversion plot was seen at temperatures between 273 and 373 K where activity dropped from 100 % conversion at 273 K to 70 % at 363 K before returning to 100 % at temperatures higher than 373 K.<sup>27</sup> One possible explanation for the "U" shape conversion plot is the presence of trace water impurities that deactivate the catalyst at ambient temperatures while operation at low temperatures serves as a cold trap for water removal and operation at high temperatures minimizes the influence of water as an inhibitor. <sup>27,51</sup> Indeed, upon purification of the gases by passing through cold traps, the "U" shape was avoided and 100 % conversion was observed at all temperatures investigated.<sup>27</sup> This inhibition contrasts with reports for some Au catalysts<sup>53-55</sup> and FeO-Pt interfaces,<sup>56</sup> where surface hydroxyl groups are known to promote the low temperature oxidation of CO. To explore the potential influence of water, we evaluated CO oxidation over Co-N-C in the presence and absence of co-fed water at 273 and 303 K. Figure S8 shows cofed water (0.05 vol %) inhibited the conversion of CO, but conversion recovered when the water addition was stopped. The inhibition of the rate by addition of 0.05 vol % H<sub>2</sub>O suggests that water is not required for low temperature CO oxidation on Co-N-C.

All the gases in our study were purified (see Methods) to minimize any impacts of water on the steady-state rate. Contrary to the report by Schüth and co-workers, 27 the "U" shape of conversion as a function of temperature remained in our study (Figs. 3 and 4). Moreover, Schüth and co-workers reported that high temperature pretreatment of a Co oxide catalyst in  $H_2$  eliminated low temperature activity (<273 K) for CO oxidation.<sup>27</sup> They hypothesized that reduction of Co<sup>3+</sup> surface species to Co<sup>2+</sup> accompanied by a loss of labile O<sup>2-</sup> species was responsible for the loss of low temperature activity.<sup>27</sup> To explore the potential influence of reducible Co species on the rate of CO oxidation, we evaluated the effect of  $H_2$  pretreatment on the steady-state reaction. As summarized in Fig. 4, an in situ pretreatment of the Co-N-C catalyst at 673 K in H₂ did not significantly influence the rate or unusual "U" shape of the conversion. Evidently, easily reducible Co species, if present, are not responsible for the CO oxidation reaction at sub-ambient temperatures, which is consistent with our XPS results that indicate a majority of the Co in Co-N-C is  $Co^{2+}$ . A comparison of the X-ray absorption near edge structure (XANES) of Co-N-C after high temperature treatment in  $H_2$  and subsequent cooling to 303 K with the XANES after CO exposure (Fig. 5) shows no change in the edge position, confirming that exposure of the catalyst to H2 or CO does not alter the oxidation state of the Co. Analysis of the extended X-ray absorption fine structure (Fig. 2 and Table 1) indicates exposure of Co-N-C to CO followed by a purge in inert gas did not result in a measurable change in the average coordination environment around Co in the sample. Evidently, the number of exposed Co ions in Co-N-C that strongly bind CO at 303 K was very low.

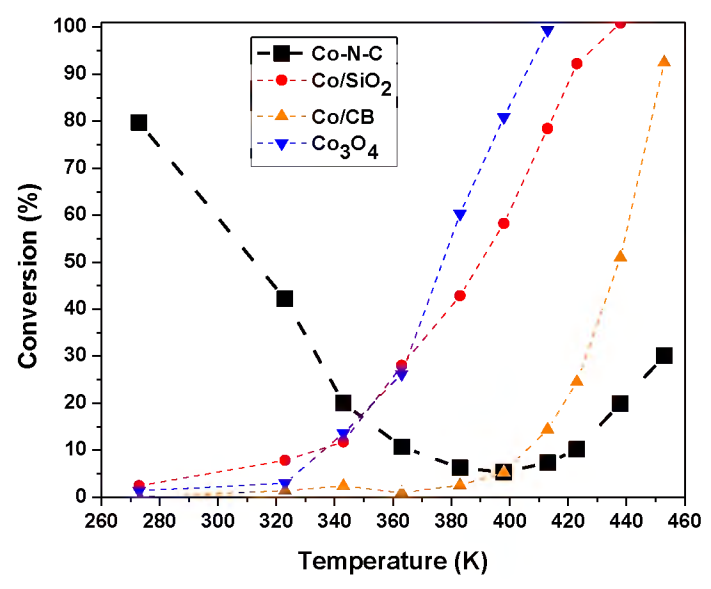


**Figure 3.** Temperature dependence of steady-state CO conversion over Co catalysts. All reactions were run with 100 mg of catalyst diluted in SiC with 160 cm $^3$  total flow, 1 % CO, 13 % O $_2$ , 1 % Ar, and balance He at 3 atm. The O $_2$  and CO lines were purified with silica traps in a dry-ice acetone bath while the He and Ar lines were purified with an OMI Filter.

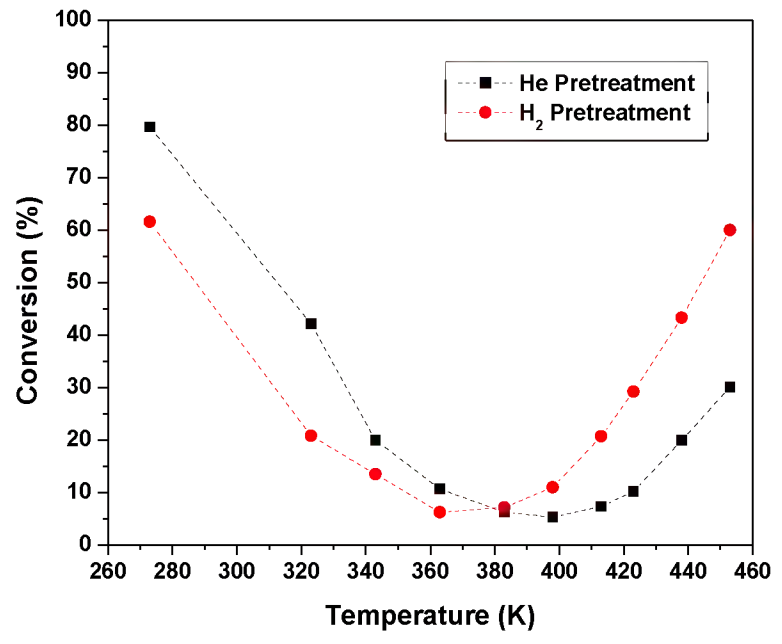


**Figure 4.** Temperature dependence of steady-state CO conversion over Co-N-C following inert or reductive pretreatment. The reactions were performed sequentially, (He followed by  $H_2$  pretreatment at 673 K) without removing the catalyst. The reaction was run with 100 mg of Co-N-C diluted in SiC and with 160 cm<sup>3</sup> total flow, 1 % CO, 13 % O<sub>2</sub>, 1 % Ar, and balance He at 3 atm. The O<sub>2</sub> and CO lines were purified with silica traps in a dry-ice acetone bath while the He and Ar lines were purified with an OMI Filter.

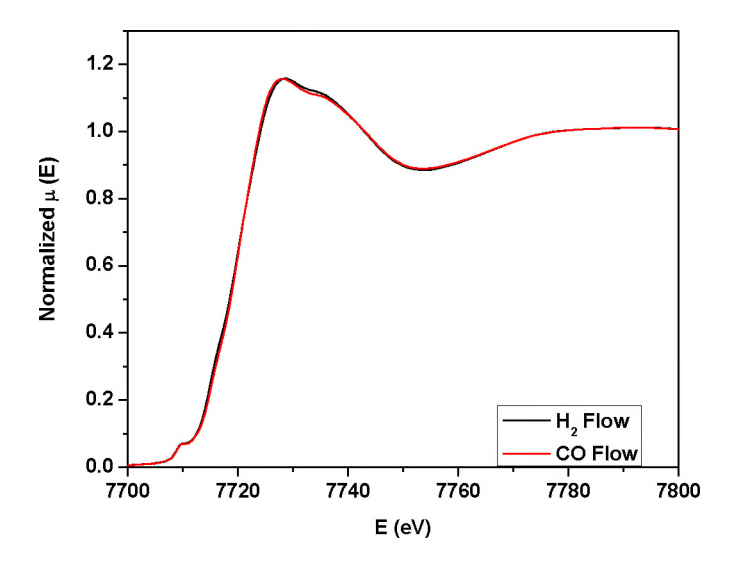


**Figure 5.** Normalized X-ray absorption near edge structure for Co-N-C. Comparison of the normalized XANES for Co-N-C under  $H_2$  and CO in situ flows (10 cm<sup>3</sup> min<sup>-1</sup>). The catalyst was initially ramped in  $H_2$  to 738 K and held for 2 hours before cooling to 303 K. The multiple scans were averaged for each XANES.

The observed orders of reaction during CO oxidation catalyzed by Co-N-C shown in Table 2 were strikingly different compared to those measured over other Co containing catalysts. The nearly first order dependence of the rate on CO observed over Co-N-C contrasts the inhibition by CO typically observed for platinum group metal catalysts that bind CO strongly.<sup>57</sup> Indeed, the positive reaction order in CO indicates binding to the active site is weak, which is consistent with the EXAFS results discussed above. The reaction orders for CO oxidation on the Co-N-C catalyst were not significantly affected by operation in the low (303 K) or high temperature regime (443 K) (Fig. S9). An attempt at investigating the kinetics at 196 K proved difficult as the activity was outside of the differential regime even when lowering the partial pressures of reactants and amount of catalyst (Fig. S10). Apart from Co-N-C, the CO reaction order measured over all the Co-containing catalysts in Table 2 was close to zero. Since Co oxide catalysts are believed to catalyze CO oxidation via an MvK type mechanism, the rate of CO reduction of the surface is rapid relative to reoxidation.<sup>27, 28, 58</sup> Interestingly, the orders of reaction in Table 2 for CO oxidation on Co-N-C are similar to those reported for isolated Ir atoms on MgAl<sub>2</sub>O<sub>4</sub>, for which an ER mechanism of CO oxidation has been postulated.<sup>21</sup>

The observed increase in the rate with lowering the temperature of CO oxidation over Co-N-C results in a negative apparent activation energy of -30 kJ mol<sup>-1</sup> in the low temperature region of Figs. 3 and 4. While high temperature CO oxidation on Co containing catalysts has been previously investigated, <sup>45</sup> the unique low temperature activity regime is relatively unexplored. To further explore the origins of the low temperature activity of CO oxidation over Co-N-C, we performed isotopic transient analysis of the steady-state reaction.

Table 2. Summary of kinetic orders for CO and  $O_2$  on various Co containing catalysts along with the apparent activation energy for CO oxidation

Catalyst	E <sub>apparent</sub> a	Orders of Reaction <sup>b</sup>		
	(kJ mol <sup>-1</sup> )	СО	$O_2$	
Co-N-C				
Low T regime	-30	0.8	0.7	
High T regime	50	0.4	0.7	
Co/SiO <sub>2</sub>	36	0.0	0.2	
Co/CB	50	0.0	0.6	
Co <sub>3</sub> O <sub>4</sub>	38	0.1	0.4	
Co <sub>3</sub> O <sub>4</sub> <sup>c</sup>	46.6	0	0.41	

- a) Apparent activation energy determined from Arrhenius-type plots shown in Figs. S11 and S12.
- b) Kinetic orders were evaluated under steady-state differential conversion (<20 %) and were determined by varying the partial pressure (from 1.5 to 4.5 kPa) of CO or O<sub>2</sub> while maintaining the other.
- c) Reference values from Perti and Kabel<sup>57</sup>

Steady-state isotopic transient kinetic analysis. As the number of active sites on the Co-N-C catalyst is unknown, a reaction rate normalized by the total Co loading may underestimate the turnover frequency (TOF) of the reaction. To better evaluate the TOF, we performed steady-state isotopic transient kinetic analysis (SSITKA) of the CO oxidation reaction, which is a kinetic method that does not require a priori knowledge of the active site density to normalize the observed rate. After achieving steady state during CO oxidation at 273 K, the reactant stream was abruptly switched to one that contains <sup>13</sup>CO instead of  $^{12}$ CO using the scheme shown in Fig. S1. More experimental details can be found in the Methods and an example switch between <sup>12</sup>CO/Ar and <sup>13</sup>CO/He during steady-state CO oxidation is shown in Fig. 6a. In brief, the integration of the areas under the product <sup>12</sup>CO<sub>2</sub> or <sup>13</sup>CO<sub>2</sub> subtracted from the tracer Ar signal gives the average residence time of surface intermediates leading to product  $(\tau)$ . The strong influence of flow rate on  $\tau$  given in Fig. 6b for the case without a co-feed of CO<sub>2</sub> indicates the rate is affected by conversion or there is a strong influence of product re-adsorption on the measured  $\tau$ . As illustrated in Fig. S2, varying the reactant flow rate changes the conversion of CO between 6 and 13 % (with no co-fed CO<sub>2</sub>), resulting in a reaction rate that is independent of conversion. Moreover, the conversion extrapolates to zero at infinite flow rate when no CO2 was co-fed. These observations are consistent with differential conversion of CO in the reactor and lack of any inhibition by product CO2 under the conditions explored. The influence of flowrate on  $\tau$  in Fig. 6b is therefore attributed to product re-adsorption in the catalyst bed. Although increasing the flowrate through the reactor bed minimizes the influence of interparticle readsorption on  $\tau$ , the flowrate does not impact re-adsorption of CO<sub>2</sub> within the catalyst pores. Thus, cofeeding an excess of <sup>12</sup>CO<sub>2</sub> can be used to outcompete the re-adsorption of product <sup>13</sup>CO<sub>2</sub> formed during a transient experiment.<sup>35, 36</sup> Interestingly, co-feeding a high level of CO<sub>2</sub> actually inhibited the global steady-state rate (see Figs. S2 and S13), suggesting competitive adsorption on active sites, which will be discussed later. Extrapolating the  $\tau$  values to infinite flowrate in the presence of co-fed CO<sub>2</sub> gives a value that is statistically close to zero (Fig. 6b), suggesting a high intrinsic turnover rate at 273 K that cannot be accurately quantified by this method. Nevertheless, using the result obtained at the highest measured flow rate and 4 % co-fed <sup>12</sup>CO<sub>2</sub> (circled point in Fig. 6b) an estimated lower bound on the turnover frequency was calculated:

$$TOF = \frac{1}{\tau} = 0.3 \ s^{-1} \tag{2}$$

A material balance on the reactor was used to estimate the upper bound on the number of adsorbed species that convert to product at the time of the switch, using the following equation involving  $\tau$  and the steady-state rate of CO oxidation:

$$N_{CO_{\gamma}} = \tau R_{CO_{\gamma}} \tag{3}$$

The upper bound of coverage  $N_{COx}$  was calculated to be 10 % of the total Co in the sample as evaluated by elemental analysis. Clearly, the high global rate of low temperature CO oxidation on Co-N-C is attributed to the high intrinsic TOF with only a small portion of the Co being covered with intermediates leading to product.

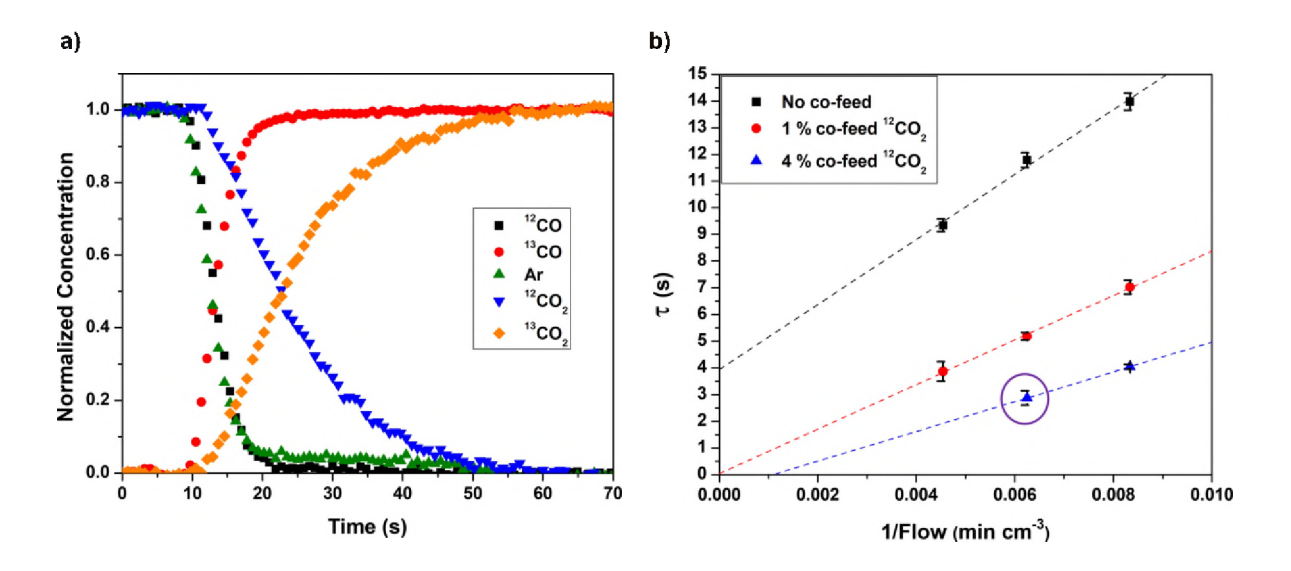


**Figure 6.** a) Example isotopic transient response following a switch from  $^{12}$ CO and  $^{13}$ CO during CO oxidation on Co-N-C. The reaction was run with 30 mg of Co-N-C diluted in SiC and with 160 cm<sup>3</sup> total flow, 1 % CO, 1 % O<sub>2</sub>, 1 % Ar, and balance He at 3 atm. The O<sub>2</sub> and CO lines were purified with silica traps submersed in a dry-ice acetone bath while the He and Ar lines were purified with an OMI Filter. The CO<sub>2</sub> line was purified by 3 Å molecular sieves. b) Effect of flow rate on the  $\tau$  with various co-feed partial pressures of  $^{12}$ CO<sub>2</sub>. The purple circled point was used to calculate lower bound of TOF and upper bound of  $N_{COX}$ . In b), the data points and error bars represent the average and standard deviation based on analysis of 3 to 6 transient response curves over a single catalyst.

Density functional theory screening of potential active sites and mechanism. The kinetic data in Table 2 and the SSITKA results suggest that both CO and O₂ bind weakly to the active site. Figure 7 shows the vdW-DF functional computed CO and O<sub>2</sub> binding energies for Co-N-C sites in the graphene plane with zero to four N coordinated to the Co ion, implicated as active sites on these materials for both ORR and oxidative dehydrogenation reactions. 4, 9, 59, 60 Full computational details are provided in Methods. Increasing the number of N coordinated to Co generally leads to a reduction in binding energy of both CO and O2. This result is consistent with previous reports that N substitutions for the C atoms that create pyridinic binding modes to a transition metal center stabilizes the d-orbitals relative to the Fermi level and thus weakens binding energies of adsorbates.<sup>45</sup> Our results also indicate that the binding energy for CO and O<sub>2</sub> on CoN<sub>4</sub> are significantly weaker than CO on Pt (-155 kJ mol<sup>-1</sup>), which has a negative CO order, in contrast to the positive CO order we observe on our Co-N-C catalyst. 61 The CoN<sub>4</sub> site is consistent with the Co<sup>2+</sup> oxidation state from XPS (Fig. S6) and coordination number from EXAFS (Table 1), is very stable relative to other Co-N-C sites, 45, 49, 62 and fits the criterion for weak binding of both reactants. Thus, even if other Co sites coordinated to less than 4 N atoms are present as minority species in our catalyst, the strong binding energy of CO on these sites is inconsistent with the observed positive CO order and low coverage of CO as a reactive intermediate inferred from SSITKA, precluding their participation in the low temperature (< 400 K) catalytic cycle. Therefore, we next investigated the mechanism for low temperature CO oxidation over the CoN<sub>4</sub> site.

Previously calculated barriers for CO oxidation on various transition metals in N-C involve direct dissociation of  $O_2$  over the metal center, which incurs large activation energies (i.e., 66 kJ mol<sup>-1</sup> on CoN<sub>4</sub>), and should alter the oxidation state of Co upon exposure to  $O_2$ .<sup>38, 45</sup> While the proposed mechanisms in those studies may explain the CO oxidation activity we observe at > 400 K (Fig. 3), they are incompatible with the activity and negative apparent activation energy observed in the low temperature kinetic regime, and also our prior in situ XAS results demonstrating no change in the Co oxidation state upon exposure to  $10\% O_2$  at 373 K.<sup>9</sup>

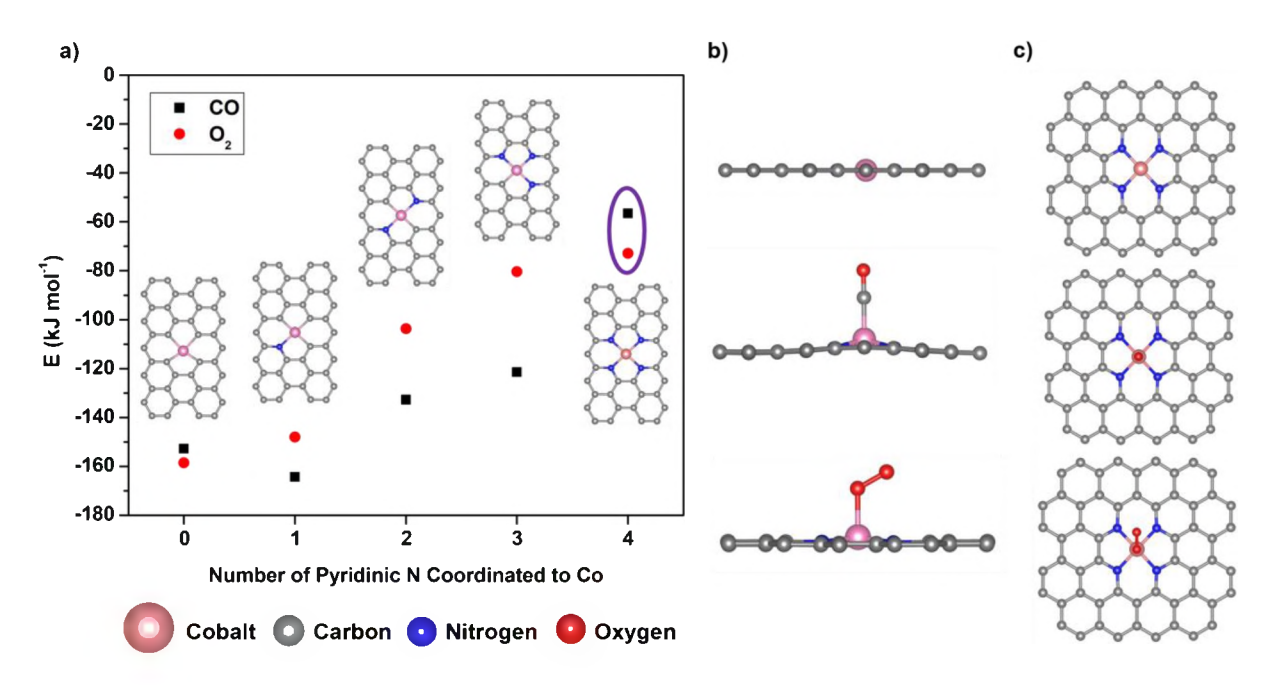


**Figure 7.** Adsorption energies were calculated using the vdW-DF functional because it shows good agreement with the experimental enthalpy of reaction for gas phase CO oxidation (Table S2). The purple circle highlights the binding energies for the CoN<sub>4</sub> structure that is displayed in b) side view and c) top down.

To explore potential configurations for simultaneous adsorption of CO and  $O_2$  we used NVT ab initio molecular dynamics (AIMD) starting from a supercell containing the  $CoN_4$  site, one CO, and one  $O_2$ ; AIMD details are in Methods, and trajectories and movies are provided in a supplemental attachment and in Fig. S5. Early in the AIMD simulation CO binds to the  $CoN_4$  site and one of the oxygen atoms in  $O_2$  becomes weakly coordinated to CO. Surprisingly, the O-O bond distance then increased upon interaction with an adjacent C in the graphene sheet, until finally breaking, leaving behind a bent O-C-O complex bound through C to the Co, and one oxygen atom bound to carbon on the N-C support (O\*). The O-C-O complex then rapidly desorbs from Co, forming a linear  $CO_2$  molecule with no bonds to Co or the support. To complete the catalytic cycle, we ran a subsequent AIMD simulation starting from the previous structure, removing the desorbed  $CO_2$ , and adding a CO molecule to the cell. The CO binds to the Co ion and subsequently reacts with O\* to form  $CO_2$  and desorb, completing the catalytic cycle. The formation of  $CO_2$  during both AIMD simulations, without the use of enhanced sampling techniques to bias structures along a prescribed reaction coordinate, suggests that these reactions occur with very low activation barriers.

Due to the similar binding energies of CO and  $O_2$ , we also repeated these two AIMD simulations starting from  $O_2$  adsorbed to the  $CoN_4$  site and did not observe any reactions during these simulations. We did not observe co-adsorption of CO and  $O_2$  to Co in any of our simulations, and geometry optimization of structures with both bound to Co resulted in desorption of either CO or  $O_2$  depending on the initial structure. To determine if  $O_2$  can bind to other surface sites in the absence of CO, we optimized structures with  $O_2$  initially located on either graphitic C with only C nearest neighbors, a C atom with a N nearest neighbor, or a N atom. Regardless of the initial guess structure, the subsequent geometry optimization for all three potential binding sites led to either movement of the  $O_2$  molecule to the CO site (yielding an analogous structure to that of  $O_2CON_4$ , shown in Figure 7b, c), or desorption of the  $O_2$  molecule from the surface. Taken together, our results indicate that for  $CoN_4$  the only two viable sites for  $O_2$  adsorption are the CO atom or a CO molecule that is bound to CO, suggesting a possible CO oxidation mechanism over  $CON_4$  sites whereby  $O_2$  dissociation is assisted by CO bound to CO and the N-C support itself.

Structures derived from the AIMD simulations were subsequently used for detailed calculations of the reaction coordinate. Figure 8 shows the resulting potential energy diagram, schematic representations, and vdW-DF computed structures. We report only energies and not free energies because the reaction intermediates are weakly adsorbed and not amenable to standard free energy approximations. Our AIMD simulation results and the similar binding energies of CO and  $O_2$  on  $CoN_4$  (Fig. 7) suggest the mechanism initiates with CO adsorbed on  $CoN_4$  (2). This is followed by weak interaction of  $O_2$  with CO (3) and subsequent dissociation of  $O_2$  upon interaction with the N-C support to form an O-O-C=O transition state (TS1) and subsequently  $O^*$  and  $CO_2$  (4). This reaction sequence is followed by adsorption of CO to Co (5). The reaction of Co-bound CO with  $O^*$  has a barrier of only 0.2 kJ mol<sup>-1</sup> (TS2), and  $CO_2$  desorbs from Co (1) to close the catalytic cycle. Throughout this reaction cascade the 16 kJ mol<sup>-1</sup> activation energy (TS1) is the only significant barrier.

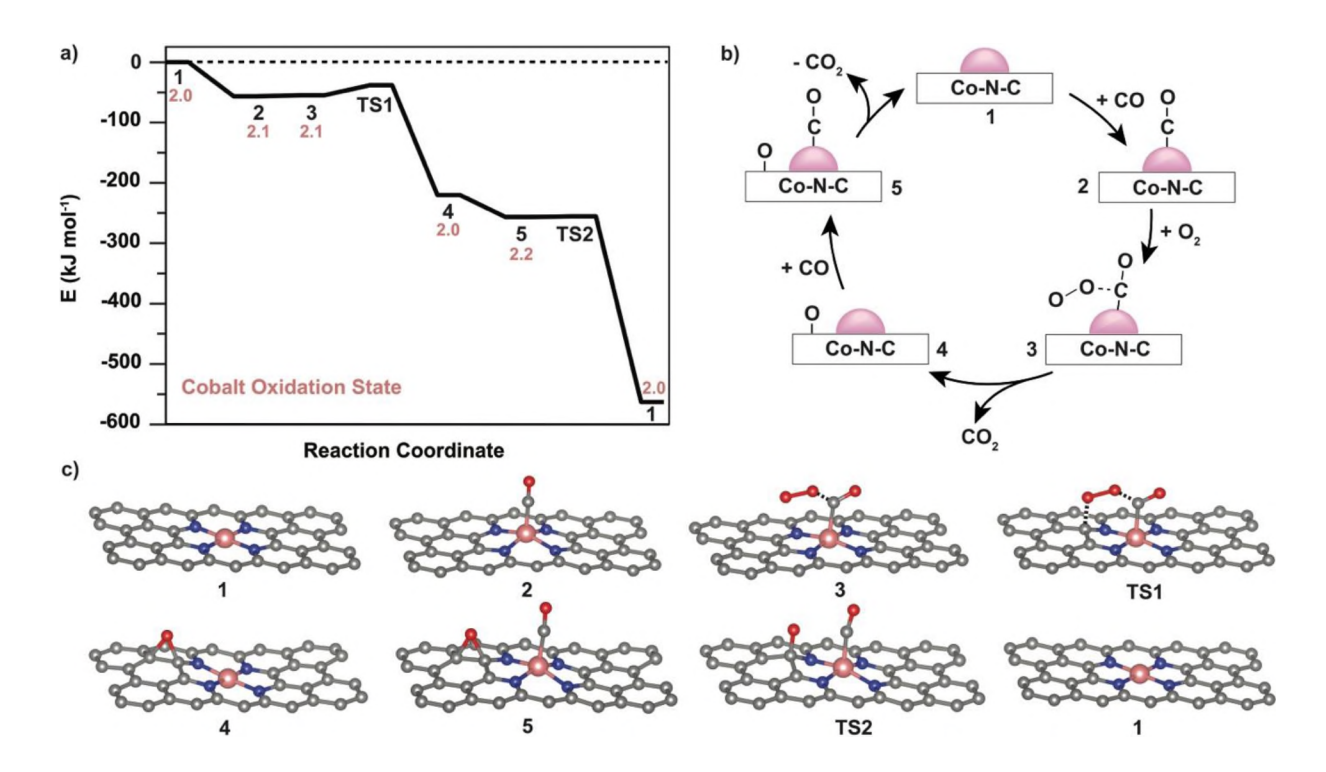


**Figure 8.** a) vdW-DF computed reaction coordinate for the complete CO oxidation mechanism over CoN<sub>4</sub>. b) Schematic of the complete catalytic cycle. c) Molecular structures corresponding to the reaction coordinate. Changes in the Co oxidation state were calculated using a normalized Bader charge analysis (Fig. S14).

Bader charge analysis (Fig. 8a and Fig. S14) confirmed that the Co remained in a  $^{2}$ + oxidation state throughout the entire reaction mechanism. The lack of change in oxidation state indicates that Co does not undergo redox during the mechanism and is consistent with the lack of influence of gaseous environment on the Co K-edge XANES (CO or  $H_2$  exposure in Fig. 5 and  $O_2$  or  $H_2$  exposure in reference 9). The weak binding of CO and  $O_2$  on the CoN<sub>4</sub> site is consistent with the positive experimental reaction orders and SSITKA results, and the low activation barrier for the rate determining step suggests that this reaction mechanism is plausible for CO oxidation in the low temperature (< 400 K) kinetic regime.

#### 4. Discussion.

The proposed reaction path is energetically downhill at every step and the elementary step involving  $O_2$  activation (through transition state TS1) has a low barrier of 16 kJ mol<sup>-1</sup> (Fig. S4 a). To explain the observed reaction kinetics (observed reaction orders and apparent negative activation energy), we need to account for the weak binding of reactants. The rate of the reaction step involving dioxygen activation (through TS-1) should be proportional to the overall reaction rate as the sequential oxidation of CO with the second oxygen atom is nearly barrierless (see results for TS-2 in Fig. S4 b). Thus, we can write an expression for the observed rate as:

$$Rate = k[CO - O_2]_{ads} (4)$$

where  $[CO-O_2]_{ads}$  represents the surface concentration of the surface complex that is formed by adsorption of CO on Co followed by very weak adsorption of  $O_2$  next to CO to give the structure depicted as 3 in Fig. 8. Although the results in Fig. 7 suggest that CO and  $O_2$  will compete for binding on the Co site and subsequent MD simulations indicate only the adsorbed CO will lead to reaction, the low coverages suggest that a first order model could be assumed. Thus, a standard Langmuir isotherm for competitive adsorption can be utilized to calculate the fractional coverage of CO on the hypothetical lattice of non-interacting Co sites  $(\theta_{CO})$  in the limit of low coverage of both CO and  $O_2$ :

$$\theta_{CO} = \frac{K_{CO}[CO]}{(1 + K_{CO}[CO] + K_{O_2}[O_2])} = K_{CO}[CO]$$
 (5)

where the K values represent the adsorption equilibrium constants of CO and O2 on bare Co ions.

Likewise, the very weak adsorption of  $O_2$  adjacent to the adsorbed CO is approximated by the linear portion of an adsorption isotherm, i.e. the adsorbed amount is proportional to the adsorption equilibrium constant of  $O_2$  next to CO ( $K_{O2}$ ') and the partial pressure of  $O_2$ . The observed rate is therefore approximated as:

$$r \propto k K_{CO} K'_{O_2}[CO][O_2] \tag{6}$$

which compares well the experimentally measured orders of reaction near unity for both CO and  $O_2$ . Using the expression in (6), the apparent activation energy ( $E_{apparent}$ ) of the CO oxidation reaction can be evaluated from the barrier to form TS1 ( $E_a$ ) and the heats of adsorption of CO adsorbed on Co and  $O_2$  adsorbed adjacent to CO according to:

$$E_{\text{apparent}} = E_a + \Delta H_{CO} + \Delta H_{CO-O_2} = -41 \, kJ \, mol^{-1}$$
 (7)

Substituting the calculated barrier of  $O_2$  activation through TS1 (16 kJ mol<sup>-1</sup>) and the binding energies from the DFT calculations (-57 for CO on Co, and  $\sim 0$  kJ mol<sup>-1</sup> for  $O_2$  adjacent to adsorbed CO) into (7), we estimate  $E_{apparent}$  = -41 kJ mol<sup>-1</sup>, which is within reasonable agreement with the experimental value of -30 kJ mol<sup>-1</sup> and is consistent with our proposed mechanism for low temperature CO oxidation.

Whereas we focused primarily on the low temperature mechanism of CO oxidation, the reaction at elevated temperature may proceed through a high barrier path that was previously reported by Mavrikakis and co-workers. Their mechanism involves dissociation of  $O_2$  on the subsequently oxidized Co site prior to reacting with CO to form two  $CO_2$  molecules. In addition, a small number of undetected Co oxide particles may also be present on the surface of Co-N-C, which could catalyze CO oxidation at elevated temperatures via the MvK mechanism known to occur with Co oxide. O(2, 10) (27, 28, 63-66)

We realize that a simplified kinetic analysis has been applied to the low temperature regime, but the model accounts for the key features of the reaction, namely the nearly first order behavior in both CO and  $O_2$  and a negative apparent activation energy. In this model, lower temperatures increase the number of adsorbed species on the surface without compromising the fast rate of  $O_2$  activation. In other words, the implication of a very low barrier for  $O_2$  activation is that the observed rate is dictated primarily by the number of adsorbed intermediates that lead to product. Furthermore, the proposed mechanism for low temperature CO oxidation over Co-N-C catalysts involves the CO-assisted activation of  $O_2$  through a O-O-C=O transition state that is similar to that proposed previously for the reaction occurring on CO-saturated Pt clusters at much higher temperatures. Under reaction conditions that saturate a Pt surface with CO,

the unavailability of adjacent surface vacancies on the Pt prevents dissociative chemisorption of  $O_2$  on the catalyst.<sup>67</sup> The reaction under those conditions is therefore proposed to proceed through a CO-assisted  $O_2$  dissociation step involving the decomposition of an O-O-C=O surface intermediate to give  $CO_2$  and a surface oxygen atom, which rapidly reacts with adsorbed CO to form another  $CO_2$ .<sup>67</sup> The barriers to form and react the proposed intermediate are quite low, consistent with the results reported here. The mechanism presented in our study is also comparable to that proposed for CO oxidation on Au stepped surfaces whereby  $O_2$  weakly binds to Au in the presence of adsorbed CO to form an  $O_2$ -CO surface intermediate that can subsequently decomposes to form  $CO_2$ .<sup>68</sup> To the best of our knowledge, these types of reactive intermediates have not been proposed previously for the low temperature oxidation of CO over Co-N-C type materials.

We attribute the low coverage of reactive intermediates leading to product, as revealed by SSITKA, to the weak binding energy of reactants to the isolated Co ions and relatively low partial pressures used in the study. Although there may be multiple motifs for Co to reside on Co-N-C, the  $CoN_4$  motif that is often proposed to be the majority species in M-N-C catalysts is entirely consistent with all of the observations reported in this work. Thus, we do not need to invoke the presence of a trace species of Co to account for the observations.

We realize the above model does not include any potential inhibition by  $CO_2$ . As shown in Fig. S2, inhibition by  $CO_2$  is not observed when the conversion of CO is differential and  $CO_2$  is not co-fed. When the concentration of  $CO_2$  was co-fed at orders of magnitude higher levels, there was an inhibitory effect on the rate as summarized in Fig. S13. This observation is entirely consistent with the model discussed above as high pressures of  $CO_2$  are expected to eventually compete for  $CO_2$  in other words, the expression for  $CO_2$  in Equation 5 can be easily modified to include competitive adsorption of  $CO_2$  on the  $CO_2$  on the  $CO_3$  in addition, the presence of high levels of  $CO_3$  could inhibit the weak interaction of  $CO_3$  with  $CO_3$  during the formation of the  $CO_3$  could complex.

# 5. Conclusions.

Our results suggest that isolated Co ions doped into nitrogen-carbon can utilize reductant molecules to activate  $O_2$  via the surrounding carbon support at low temperatures. Further, both our calculations and experiments suggest Co maintains a 2+ oxidation state upon exposure to the reaction gas mixture or individual components of it, completing the catalytic reaction without undergoing a redox cycle between  $Co^{2+}$  and  $Co^{3+}$ . Since the metal ion is not required to undergo a redox cycle to facilitate the reaction, we anticipate that further studies on other metal ions in N-C could yield similar results.

### **Competing interests**

The authors declare no competing interests.

## **Supporting Information**

The Supporting Information is available free of charge at:

Supporting information: Additional results pertaining to both experimental and computational work presented: the reactor schematic, effect of flow rate and CO<sub>2</sub> partial pressure on the CO oxidation rate during SSITKA, computed binding energies for adsorbates on Co in different cell sizes, the effect of functional on gas phase and binding energies, potential energy diagrams, NEB calculations, NVT-AIMD simulation information, XPS plots, low temperature activity plot for Co-N-C, Arrhenius plots for various Co catalysts, and Bader charges plotted over the reaction coordinate (S1); geometries of all computed species (S2); trajectory files from AIMD runs (S3); and movie files from both AIMD simulations (S4).

### Acknowledgements

This research was sponsored by the U.S. National Science Foundation under grant # CBET-1802482. C.P. acknowledges the donors of the American Chemical Society Petroleum Research Fund for partial support of this research. This research used beamline 8-ID of the National Synchrotron Light Source II, a U.S. Department of Energy (DOE) Office of Science User Facility operated for the DOE Office of Science by Brookhaven National Laboratory under Contract No. DE-SC0012704. Dr. Eli Stavitski provided technical assistance with operating beamline 8-ID. Scanning Transmission Electron Microscopy research was conducted as part of a user project at the Center for Nanophase Materials Sciences (CNMS), which is a US Department of Energy, Office of Science User Facility at Oak Ridge National Laboratory. Helpful technical discussions with Sugandha Verma and Dr. Gordon Brezicki are also acknowledged.

#### References

- 1. Liang, H. W.; Wei, W.; Wu, Z. S.; Feng, X.; Müllen, K. Mesoporous Metal-Nitrogen-Doped Carbon Electrocatalysts for Highly Efficient Oxygen Reduction Reaction. *J. Am. Chem. Soc.* **2013**, *135* (43), 16002-16005. DOI: 10.1021/ja407552k
- 2. Liu, Q.; Zhang, J. Graphene Supported Co-g- $C_3N_4$  as a Novel Metal-Macrocyclic Electrocatalyst for the Oxygen Reduction Reaction in Fuel Cells. *Langmuir* **2013**, *29* (11), 3821-3828. DOI: 10.1021/la400003h
- 3. Malko, D.; Kucernak, A.; Lopes, T. In Situ Electrochemical Quantification of Active Sites in Fe-N/C Non-Precious Metal Catalysts. *Nat. Commun.* **2016**, *7*, 1-7. DOI: 10.1038/ncomms13285
- 4. Zitolo, A.; Ranjbar-Sahraie, N.; Mineva, T.; Li, J.; Jia, Q.; Stamatin, S.; Harrington, G. F.; Lyth, S. M.; Krtil, P.; Mukerjee, S.; Fonda, E.; Jaouen, F. Identification of Catalytic Sites in Cobalt-Nitrogen-Carbon Materials for the Oxygen Reduction Reaction. *Nat. Commun.* **2017**, *8*, 957. DOI: 10.1038/s41467-017-01100-7
- 5. Zhang, Q.; Mamtani, K.; Jain, D.; Ozkan, U.; Asthagiri, A. CO Poisoning Effects on FeNC and  $CN_x$  ORR Catalysts: A Combined Experimental–Computational Study. *J. Phys. Chem. C* **2016**, *120* (28), 15173-15184. DOI: 10.1021/acs.jpcc.6b03933
- 6. Jain, D.; Zhang, Q.; Hightower, J.; Gustin, V.; Asthagiri, A.; Ozkan, U. S. Changes in Active Sites on Nitrogen-Doped Carbon Catalysts Under Oxygen Reduction Reaction: A Combined Post-Reaction Characterization and DFT Study. *ChemCatChem* **2019**, *11* (24), 5945-5950. DOI: 10.1002/cctc.201901883
- 7. Vijay, S.; Ju, W.; Brückner, S.; Tsang, S. C.; Strasser, P.; Chan, K. Unified Mechanistic Understanding of CO<sub>2</sub> Reduction to CO on Transition Metal and Single Atom Catalysts. *Nat. Catal.* **2021**, *4*, 1024-1031. DOI: 10.1038/s41929-021-00705-y
- 8. Xie, J.; Yin, K.; Serov, A.; Artyushkova, K.; Pham, H. N.; Sang, X.; Unocic, R. R.; Atanassov, P.; Datye, A. K.; Davis, R. J. Selective Aerobic Oxidation of Alcohols over Atomically-Dispersed Non-Precious Metal Catalysts. *ChemSusChem* **2017**, *10* (2), 359-362. DOI: 10.1002/cssc.201601364
- 9. Xie, J.; Kammert, J. D.; Kaylor, N.; Zheng, J. W.; Choi, E.; Pham, H. N.; Sang, X.; Stavitski, E.; Attenkofer, K.; Unocic, R. R.; Datye, A. K.; Davis, R. J. Atomically Dispersed Co and Cu on N-Doped Carbon for Reactions Involving C–H Activation. *ACS Catal.* **2018**, *8* (5), 3875-3884. DOI: 10.1021/acscatal.8b00141
- 10. Huang, K.; Fu, H.; Shi, W.; Wang, H.; Cao, Y.; Yang, G.; Peng, F.; Wang, Q.; Liu, Z.; Zhang, B.; Yu, H. Competitive Adsorption on Single-Atom Catalysts: Mechanistic Insights into the Aerobic Oxidation of Alcohols over Co–N–C. *J. Catal.* **2019**, *377*, 283-292. DOI: 10.1016/j.jcat.2019.06.047
- 11. Liao, C.; Li, X.; Yao, K.; Yuan, Z.; Chi, Q.; Zhang, Z. Efficient Oxidative Dehydrogenation of N-Heterocycles over Nitrogen-Doped Carbon-Supported Cobalt Nanoparticles. *ACS Sustain. Chem. Eng.* **2019**, *7* (16), 13646-13654. DOI: 10.1021/acssuschemeng.8b05563
- 12. Li, J.; Liu, J.; Zhang, J.; Wan, T.; Huang, L.; Wang, X.; Pan, R.; An, Z.; Vlachos, D. G. An Unconventional DCO<sub>x</sub> Favored Co/N-C Catalyst for Efficient Conversion of Fatty Acids and Esters to Liquid Alkanes. *Appl. Catal.*, A **2020**, *591*, 117385-117394. DOI: 10.1016/j.apcata.2019.117385
- 13. Shao, M.; Chang, Q.; Dodelet, J.-P.; Chenitz, R. Recent Advances in Electrocatalysts for Oxygen Reduction Reaction. *Chem. Rev.* **2016**, *116* (6), 3594-3657. DOI: 10.1021/acs.chemrev.5b00462
- 14. Wang, J.; You, R.; Zhao, C.; Zhang, W.; Liu, W.; Fu, X. P.; Li, Y.; Zhou, F.; Zheng, X.; Xu, Q.; Yao, T.; Jia, C. J.; Wang, Y. G.; Huang, W.; Wu, Y. N-Coordinated Dual-Metal Single-Site Catalyst for Low-Temperature CO Oxidation. *ACS Catal.* **2020**, *10* (4), 2754-2761. DOI: 10.1021/acscatal.0c00097
- 15. Luo, F.; Choi, C. H.; Primbs, M. J. M.; Ju, W.; Li, S.; Leonard, N. D.; Thomas, A.; Jaouen, F.; Strasser, P. Accurate Evaluation of Active-Site Density (SD) and Turnover Frequency (TOF) of PGM-Free Metal-Nitrogen-Doped Carbon (MNC) Electrocatalysts using CO Cryo Adsorption. *ACS Catal.* **2019**, *9* (6), 4841-4852. DOI: 10.1021/acscatal.9b00588
- 16. Luo, F.; Wagner, S.; Onishi, I.; Selve, S.; Li, S.; Ju, W.; Wang, H.; Steinberg, J.; Thomas, A.; Kramm, U. I.; Strasser, P. Surface Site Density and Utilization of Platinum Group Metal (PGM)-Free Fe-NC

- and FeNi-NC Electrocatalysts for the Oxygen Reduction Reaction. *Chem. Sci.* **2021,** *12*, 384-396. DOI: 10.1039/D0SC03280H
- 17. Bamwenda, G. R.; Tsubota, S.; Nakamura, T.; Haruta, M. The Influence of the Preparation Methods on the Catalytic Activity of Platinum and Gold Supported on TiO<sub>2</sub> for CO Oxidation. *Catal. Lett.* **1997**, *44*, 83-87. DOI: 10.1023/A:1018925008633
- 18. Berlowitz, P. J.; Peden, C. H. F.; Goodman, D. W. Kinetics of CO Oxidation on Single-Crystal Pd, Pt, and Ir. *J. Phys. Chem.* **1988**, *92* (18), 5213-5221. DOI: 10.1021/j100329a030
- 19. Mars, P.; van Krevelen, D. W. Oxidations Carried out by Means of Vanadium Oxide Catalysts. *Chem. Eng. Sci.* **1954**, *3*, 41-59. DOI: 10.1016/S0009-2509(54)80005-4
- 20. Close, J. S.; White, J. M. On the Oxidation of Carbon Monoxide Catalyzed by Palladium. *J. Catal.* **1975,** *36* (2) 185-198. DOI: 10.1016/0021-9517(75)90023-8
- 21. Lu, Y.; Wang, J.; Yu, L.; Kovarik, L.; Zhang, X.; Hoffman, A. S.; Gallo, A.; Bare, S. R.; Sokaras, D.; Kroll, T.; Dagle, V.; Xin, H.; Karim, A. M. Identification of the Active Complex for CO Oxidation over Single-Atom Ir-on-MgAl<sub>2</sub>O<sub>4</sub> Catalysts. *Nat. Catal.* **2019**, *2*, 149-156. DOI: 10.1038/s41929-018-0192-4
- 22. Haruta, M. Size- and Support-Dependency in the Catalysis of Gold. *Catal. Today* **1997**, *36* (1), 153-166. DOI: 10.1016/S0920-5861(96)00208-8
- 23. Haruta, M.; Kobayashi, T.; Sano, H.; Yamada, N. Novel Gold Catalysts for the Oxidation of Carbon Monoxide at a Temperature far Below 0 °C. *Chem. Lett.* **1987**, *16* (2). 405-408. DOI: 10.1246/cl.1987.405
- 24. Haruta, M.; Tsubota, S.; Kobayashi, T.; Kageyama, H.; Genet, M. J.; Delmon, B. Low-Temperature Oxidation of CO over Gold Supported on TiO<sub>2</sub>,  $\alpha$ -Fe<sub>2</sub>O<sub>3</sub>, and Co<sub>3</sub>O<sub>4</sub>. *J. Catal.* **1993**, *144* (1), 175-192. DOI: 10.1006/jcat.1993.1322
- 25. Jansson, J.; Palmqvist, A. E. C.; Fridell, E.; Skoglundh, M.; Österlund, L.; Thormählen, P.; Langer, V. On the Catalytic Activity of Co<sub>3</sub>O<sub>4</sub> in Low-Temperature CO Oxidation. *J. Catal.* **2002**, *211* (2), 387-397. DOI: 10.1006/jcat.2002.3738
- 26. Zheng, J.; Chu, W.; Zhang, H.; Jiang, C.; Dai, X. CO Oxidation over Co<sub>3</sub>O<sub>4</sub>/SiO<sub>2</sub> Catalysts: Effects of Porous Structure of Silica and Catalyst Calcination Temperature. *J. Nat. Gas Chem.* **2010**, *19* (6), 583-588. DOI: 10.1016/S1003-9953(09)60119-5
- 27. Gu, D.; Jia, C. J.; Weidenthaler, C.; Bongard, H. J.; Spliethoff, B.; Schmidt, W.; Schüth, F. Highly Ordered Mesoporous Cobalt-Containing Oxides: Structure, Catalytic Properties, and Active Sites in Oxidation of Carbon Monoxide. *J. Am. Chem. Soc.* **2015**, *137* (35), 11407-11418. DOI: 10.1021/jacs.5b06336
- 28. Baidya, T.; Murayama, T.; Nellaiappan, S.; Katiyar, N. K.; Bera, P.; Safonova, O.; Lin, M.; Priolkar, K. R.; Kundu, S.; Srinivasa Rao, B.; Steiger, P.; Sharma, S.; Biswas, K.; Pradhan, S. K.; Lingaiah, N.; Malviya, K. D.; Haruta, M. Ultra-Low-Temperature CO Oxidation Activity of Octahedral Site Cobalt Species in Co₃O₄ Based Catalysts: Unravelling the Origin of the Unique Catalytic Property. *J. Phys. Chem. C* **2019**, *123* (32), 19557-19571. DOI: 10.1021/acs.jpcc.9b04136
- 29. Cai, Y.; Xu, J.; Guo, Y.; Liu, J. Ultrathin, Polycrystalline, Two-Dimensional Co<sub>3</sub>O<sub>4</sub> for Low-Temperature CO Oxidation. *ACS Catal.* **2019**, *9* (3), 2558-2567. DOI: 10.1021/acscatal.8b04064
- 30. Jagadeesh, R. V.; Junge, H.; Pohl, M.-m.; Radnik, J.; Bru, A.; Beller, M. Selective Oxidation of Alcohols to Esters Using Heterogeneous  $Co_3O_4$ –N@C Catalysts under Mild Conditions. *J. Am. Chem. Soc.* **2013**, *135* (29), 10776-10782. DOI: 10.1021/ja403615c
- 31. Lam, Y. L.; Boudart, M. Preparation of Small Au-Pd Particles on Silica. *J. Catal.* **1977,** *50* (3), 530-540. DOI: 10.1016/0021-9517(77)90064-1
- 32. Kaylor, N.; Xie, J.; Kim, Y.-S.; Pham, H. N.; Datye, A. K.; Lee, Y.-K.; Davis, R. J. Vapor Phase Deoxygenation of Heptanoic Acid over Silica-Supported Palladium and Palladium-Tin Catalysts. *J. Catal.* **2016**, *344*, 202-212. DOI: 10.1016/j.jcat.2016.09.028

- 33. Kammert, J. D.; Brezicki, G.; Acevedo-Esteves, R.; Stavitski, E.; Davis, R. J. High-Throughput Operando-Ready X-ray Absorption Spectroscopy Flow Reactor Cell for Powder Samples. *Rev. Sci. Instrum.* **2020**, *91*, 013107. DOI: 10.1063/1.5124301
- 34. Ravel, B.; Newville, M. ATHENA, ARTEMIS, HEPHAESTUS: Data Analysis for X-ray Absorption Spectroscopy using IFEFFIT. *J. Synchrotron Radiat.* **2005**, *12*, 537-541. DOI: 10.1107/S0909049505012719
- 35. Shannon, S. L.; Goodwin, J. G. Characterization of Catalytic Surfaces by Isotopic-Transient Kinetics during Steady-State Reaction. *Chem. Rev.* **1995**, *95* (3) 677-695. DOI: 10.1021/cr00035a011
- 36. Calla, J.; Bore, M.; Datye, A.; Davis, R. Effect of Alumina and Titania on the Oxidation of CO over Au Nanoparticles Evaluated by <sup>13</sup>C Isotopic Transient Analysis. *J. Catal.* **2006**, *238* (2), 458-467. DOI: 10.1016/j.jcat.2006.01.009
- 37. Kresse, G.; Furthmuller, J. Efficient Iterative Schemes for Ab Initio Total-Energy Calculations using a Plane-Wave Basis Set. *J. Phys. Rev. B* **1996**, *54* (16), 11169-11186. DOI: 10.1103/PhysRevB.54.11169
- 38. Deng, Q.; Zhao, L.; Gao, X.; Zhang, M.; Luo, Y.; Zhao, Y. Single Layer of Polymeric Cobalt Phthalocyanine: Promising Low-Cost and High-Activity Nanocatalysts for CO Oxidation. *Small* **2013**, *9* (20), 3506-3513. DOI: 10.1002/smll.201300652
- 39. Patel, A. M.; Ringe, S.; Siahrostami, S.; Bajdich, M.; Nørskov, J. K.; Kulkarni, A. R. Theoretical Approaches to Describing the Oxygen Reduction Reaction Activity of Single-Atom Catalysts. *J. Phys. Chem. C* **2018**, *122* (51), 29307-29318. DOI: 10.1021/acs.jpcc.8b09430
- 40. Dion, M.; Rydberg, H.; Schroder, E.; Langreth, D. C.; Lundqvist, B. I. van der Waals Density Functional for General Geometries. *Phys. Rev. Lett.* **2004,** *92,* 246401. DOI: 10.1103/PhysRevLett.92.246401
- 41. Perdew, J. P.; Wang, Y. Accurate and Simple Analytic Representation of the Electron-Gas Correlation Energy. *Phys. Rev. B* **1992**, *45* (23), 13244-13249. DOI: 10.1103/PhysRevB.45.13244
- 42. Lee, K.; Murray, É. D.; Kong, L.; Lundqvist, B. I.; Langreth, D. C. Higher-Accuracy van der Waals Density Functional. *Phys. Rev. B* **2010**, *82*, 3-6. DOI: 10.1103/physrevb.82.081101
- 43. Henkelman, G.; Uberuaga, B. P.; Josson, H. A Climbing Image Nudged Elastic Band Method for Finding Saddle Points and Minimum Energy Paths and Minimum Energy Paths. *J. Chem. Phys.* **2000**, *113*, 9901-9904. DOI: 10.1063/1.1329672
- 44. Henkelman, G.; Josson, H. Improved Tangent Estimate in the Nudged Elastic Band Method for Finding Minimum Energy Paths and Saddle Points. *J. Chem. Phys.* **2000**, *133*, 9978-9985. DOI: 10.1063/1.1323224
- 45. Kropp, T.; Mavrikakis, M. Transition Metal Atoms Embedded in Graphene: How Nitrogen Doping Increases CO Oxidation Activity. *ACS Catal.* **2019**, *9* (8), 6864-6868. DOI: 10.1021/acscatal.9b01944
- 46. Liu, W.; Zhang, L.; Yan, W.; Liu, X.; Yang, X.; Miao, S.; Wang, W.; Wang, A.; Zhang, T. Single-Atom Dispersed Co-N-C Catalyst: Structure Identification and Performance for Hydrogenative Coupling of Nitroarenes. *Chem. Sci.* **2016**, *7* (9), 5758-5764. DOI: 10.1039/C6SC02105K
- 47. Biesinger, M. C.; Payne, B. P.; Grosvenor, A. P.; Lau, L. W. M.; Gerson, A. R.; Smart, R. S. C. Resolving Surface Chemical States in XPS Analysis of First Row Transition Metals, Oxides and Hydroxides: Cr, Mn, Fe, Co and Ni. *Appl. Surf. Sci.* **2011**, *257* (7), 2717-2730. DOI: 10.1016/j.apsusc.2010.10.051
- 48. Haque, E.; Zavabeti, A.; Uddin, N.; Wang, Y.; Rahim, M. A.; Syed, N.; Xu, K.; Jannat, A.; Haque, F.; Zhang, B. Y.; Shoaib, M. A.; Shamsuddin, S.; Nurunnabi, M.; Minett, A. I.; Ou, J. Z.; Harris, A. T. Deciphering the Role of Quaternary N in O<sub>2</sub> Reduction over Controlled N-Doped Carbon Catalysts. *Chem. Mater.* **2020**, *32* (4), 1384-1392. DOI: 10.1021/acs.chemmater.9b03354
- 49. Ebikade, E. O.; Wang, Y.; Samulewicz, N.; Hasa, B.; Vlachos, D. Active Learning-Driven Quantitative Synthesis—Structure—Property Relations for Improving Performance and Revealing Active Sites of Nitrogen-Doped Carbon for the Hydrogen Evolution Reaction. *React. Chem. Eng.* **2020**, *5* (12), 2134-2147. DOI: 10.1039/D0RE00243G

- 50. Sun, Y.; Li, S.; Jovanov, Z. P.; Bernsmeier, D.; Wang, H.; Paul, B.; Wang, X.; Kühl, S.; Strasser, P. Structure, Activity, and Faradaic Efficiency of Nitrogen-Doped Porous Carbon Catalysts for Direct Electrochemical Hydrogen Peroxide Production. *ChemSusChem* **2018**, *11* (19), 3388-3395. DOI: 10.1002/cssc.201801583
- 51. Wang, Y.; Chen, Z.; Fang, R.; Li, Y. Hollow- $Co_3O_4@Co_3O_4@SiO_2$  Multi-Yolk-Double-Shell Nanoreactors for Highly Efficient CO Oxidation. *ChemCatChem* **2019**, *11* (2), 772-779. DOI: 10.1002/cctc.201801484
- 52. Iablokov, V.; Barbosa, R.; Pollefeyt, G.; Van Driessche, I.; Chenakin, S.; Kruse, N. Catalytic CO Oxidation over Well-Defined Cobalt Oxide Nanoparticles: Size-Reactivity Correlation. *ACS Catal.* **2015**, *5* (10), 5714-5718. DOI: 10.1021/acscatal.5b01452
- 53. Calla, J. T.; Davis, R. J., Influence of Dihydrogen and Water Vapor on the Kinetics of CO Oxidation over Au/Al<sub>2</sub>O<sub>3</sub>. *Ind. Eng. Chem. Res.* **2005**, *44*, 5403-5410. DOI: 10.1021/ie0492202
- 54. Daté, M.; Okumura, M.; Tsubota, S.; Haruta, M. Vital Role of Moisture in the Catalytic Activity of Supported Gold Nanoparticles. *Angew. Chem. Int. Ed.* **2004,** *43* (16), 2129-2132. DOI: 10.1002/anie.200453796
- 55. Saavedra, J.; Doan, H. A.; Pursell, C. J.; Grabow, L. C.; Chandler, B. D. The Critical Role of Water at the Gold-Titania Interface in Catalytic CO Oxidation. *Science* **2014**, *345* (6204), 1599-1602. DOI: 10.1126/science.1256018
- 56. Jin, Y.; Sun, G.; Xiong, F.; Wang, Z.; Huang, W. Proton-Transfer-Connected Elementary Surface Reaction Network for Low-Temperature CO Oxidation Catalyzed by Metal-Oxide Nanocatalysts. *J. Phys. Chem. C* **2016**, *120* (47) 26968-26973. DOI: 10.1021/acs.jpcc.6b10789
- 57. Perti, D; Kabel, R. L. Kinetics of CO Oxidation Over Co<sub>3</sub>O<sub>4</sub>/Al<sub>2</sub>O<sub>3</sub>. *AIChE J.* **1985,** *31* (9), 1420-1426. DOI: 10.1002/aic.690310903
- 58. Lukashuk, L.; Yigit, N.; Rameshan, R.; Kolar, E.; Teschner, D.; Hävecker, M.; Knop-Gericke, A.; Schlögl, R.; Föttinger, K.; Rupprechter, G. Operando Insights into CO Oxidation on Cobalt Oxide Catalysts by NAP-XPS, FTIR, and XRD. ACS Catal. **2018**, 8 (9), 8630-8641. DOI: 10.1021/acscatal.8b01237
- 59. Gadipelli, S.; Zhao, T.; Shevlin, S. A.; Guo, Z. Switching Effective Oxygen Reduction and Evolution Performance by Controlled Graphitization of a Cobalt–Nitrogen–Carbon Framework System. *Energy Environ. Sci.* **2016**, *9*, 1661-1667. DOI: 10.1039/C6EE00551A
- 60. Xie, X.; He, C.; Li, B.; He, Y.; Cullen, D. A.; Wegener, E. C.; Kropf, A. J.; Martinez, U.; Cheng, Y.; Engelhard, M. H.; Bowden, M. E.; Song, M.; Lemmon, T.; Li, X. S.; Nie, Z.; Liu, J.; Myers, D. J.; Zelenay, P.; Wang, G.; Wu, G.; Ramani, V.; Shao, Y. Performance Enhancement and Degradation Mechanism Identification of a Single-Atom Co–N–C Catalyst for Proton Exchange Membrane Fuel Cells. *Nat. Catal.* **2020**, *3* (12), 1044-1054. DOI: 10.1038/s41929-020-00546-1
- 61. Koper, M. T. M.; Shubina, T. E.; Santen, R. A. V. Periodic Density Functional Study of CO and OH Adsorption on Pt-Ru Alloy Surfaces: Implications for CO Tolerant Fuel Cell Catalysts. **2002**, *106*, 686-692.
- 62. Kattel, S.; Wang, G. Reaction Pathway for Oxygen Reduction on FeN₄ Embedded Graphene. *J. Phys. Chem. B* **2014**, *106* (3), 452-6. DOI: 10.1021/jp0134188
- 63. Molavi, R.; Safaiee, R.; Sheikhi, M. H.; Hassani, N. Theoretical Perspective on CO Oxidation over Small Cobalt Oxide Clusters. *Chem. Phys. Lett.* **2021**, *767* (16), 138361. DOI: 10.1016/j.cplett.2021.138361
- 64. Broqvist, P.; Panas, I.; Persson, H. A DFT Study on CO Oxidation over Co<sub>3</sub>O<sub>4</sub>. *J. Catal.* **2002**, *210* (1), 198-206. DOI: 10.1006/jcat.2002.3678
- 65. Xie, Y.; Dong, F.; Heinbuch, S.; Rocca, J. J.; Bernstein, E. R. Oxidation Reactions on Neutral Cobalt Oxide Clusters: Experimental and Theoretical Studies. *Phys. Chem. Chem. Phys.* **2010**, *12* (4), 947-959. DOI: 10.1039/B915590B
- 66. Xu, X. L.; Li, J. Q. DFT Studies on H<sub>2</sub>O Adsorption and its Effect on CO Oxidation over Spinel Co<sub>3</sub>O<sub>4</sub> (110) Surface. *Surf. Sci.* **2011**, *605* (23), 1962-1967. DOI: 10.1016/j.susc.2011.07.013

- 67. Allian, A. D.; Takanabe, K.; Fujdala, K. L.; Hao, X.; Truex, T. J.; Cai, J.; Buda, C.; Neurock, M.; Iglesia, E. Chemisorption of CO and Mechanism of CO Oxidation on Supported Platinum Nanoclusters. *J. Am. Chem. Soc.* **2011**, *133* (12), 4498-4517. DOI: 10.1021/ja110073u
- 68. Liu, Z. P.; Hu, P.; Alavi, A. Catalytic Role of Gold in Gold-Based Catalysts: A Density Functional Theory Study on the CO Oxidation on Gold. *J. Am. Chem. Soc.* **2002**, *124* (49), 14770-14779. DOI: 10.1021/ja0205885

# **For Table of Contents Only**

